Article

Aerodynamic Performance of VAWT Airfoils: Comparison between Wind Tunnel Testing Using a New Three-Component Strain Gauge Balance and CFD Modelling

Luis Santamaría, Mónica Galdo Vega [ID]**, Adrián Pandal** [ID]**, José González Pérez** [ID]**, Sandra Velarde-Suárez** [ID] **and Jesús Manuel Fernández Oro *** [ID]

Fluid Mechanics Area, Department of Energy, University of Oviedo, C/Wifredo Ricart s/n, 33204 Gijon, Asturias, Spain
* Correspondence: jesusfo@uniovi.es

Abstract: Vertical axis wind turbines are an emerging and in-development wind energy technology which are characterized by their complicated aerodynamics. Detached flow conditions, which are typically developed at operational tip speed ratios, demand a rigorous characterization of the airfoils for an accurate prediction of the turbine performance. In this work, a custom-built, three-component external strain gauge balance, specifically developed for airfoil testing, is validated. The physical reasons responsible for discrepancies with reference data are also analyzed. Two- and three-dimensional flat plates, as well as the DU06-W-200 airfoil, are tested in a wind tunnel. Lift and drag coefficients and pitching moments are obtained for a wide angular range at Re = 200,000. The results are compared with data from the bibliography and CFD simulations, performed with the recently developed GEKO (generalized k-omega) turbulence model, achieving remarkable agreement. Instantaneous forces are also analyzed with both experimental and CFD techniques, providing interesting results of the unsteady fluid dynamics. Finally, critical factors affecting the measurements are identified and enhancements are proposed for future works. In summary, a thorough evaluation of this new balance design is provided, showing its valuable potential for VAWT applications.

Keywords: airfoil testing; strain gauge balance; wind tunnel; GEKO turbulence model; vertical axis wind turbine; VAWT

1. Introduction

At the present time, humanity is focused on the achievement of a reliable, affordable, and decarbonized energy system. The accomplishment of this goal involves undoubtedly the use of renewable energy, with wind energy harvested through horizontal axis wind turbines (HAWTs) leading the way due to their mature development.

However, such objectives start to require rapid actions and deeper strategies to fulfill the established deadlines (such as a net-zero-emissions scenario by 2050 [1]). These may even include the consideration of the real-time demand curves and on-site production for self-consumption. In this regard, wind energy production in urban environments is gaining much attention. In such restrictive placements, the lift-type vertical axis wind turbines (VAWT) seem to be the best candidates for wind energy extraction [2,3] due to their omnidirectionality, avoiding the need for orientation mechanisms; their ability to work better in variable wind conditions; and their lower noise emission [4].

Nevertheless, in contrast with the well-established HAWTs, which present higher efficiencies and superior rated power, the VAWT turbines are machines still requiring a vast amount of research to overcome the crucial issues that prevent them from achieving a profitable and efficient development status [5]. First of all, their aerodynamics are far more complicated than conventional turbines and there is no agreement yet on the best reference rotor design [6]; additionally, the application on urban environments means

facing very-poor-quality wind resources [2,7]. As a result, recent efforts in this field have been directed towards increasing performance and overall energy production through the development of both flow augmentation and control devices [8]; although, the latter are even more attractive for higher-size turbines such as those for deep-water offshore environments. Therefore, a necessary first stage comprises the study of new airfoil designs (which include these characteristics) or existing airfoils in new set-ups, both requiring a precise determination of the aerodynamic properties.

To that extent, CFD methods are a highly valuable tool to improve understanding of the airflow around the turbine blades, the interactions with the flow control devices, and the effect of power augmentation devices. Moreover, they allow the analysis of different types of geometries at a lower cost. However, the accuracy of CFD simulations depends significantly on the selection of the appropriate turbulence model, computational grid construction, and numerical characteristics (temporal and spatial schemes). For that reason, experimental validation is always required. Wind tunnel testing is widely employed, although this technique faces some intrinsic problems such as prototype–tunnel interaction (blockage) which usually forces downscaling. This in turn derives from other issues, as an intensified relevance of surface roughness [9] and the increased difficulty of measuring airfoil drag at low incidence angles [10]. Furthermore, unsteady phenomena may arise due to complex aerodynamics in cases of highly loaded airfoils. This is especially relevant for VAWT turbines where high angles of attack occur, even when flow control devices are used [11]. During the regular operation of a VAWT, i.e., during a complete rotor turn, the blade angle of attack varies continuously going from positive to negative incidences of the relative incoming flow. Thus, in the pursuit of VAWT performance enhancement, or to properly design passive flow control devices, the understanding of airfoil behavior at different angles of attack is essential. To this effect, the development of accurate, reliable and affordable equipment, useful for this purpose, is inherently interesting.

Aerodynamic performance can be estimated from the integration of the pressure distributions measured with pressure taps [12] or directly with an aerodynamic balance. The first method provides more information but limits the number of geometries that can be tested, as every prototype has to be complexly manufactured to include the pressure tabs and tubes. On the other hand, while there are a wide variety of balance designs, external balances (placed outside the test section) are the most common for airfoil testing. Within external balances, two types are distinguished, single-piece (with multi-component load cells) and multi-piece (with several load cells) [13]. Single-piece aerodynamic balances are usually expensive and not commercial, as each application usually requires a specific range distribution; thus, they are custom-manufactured [14]. Meanwhile, multi-piece balances typically need more space, although in external balances, that is not commonly problematic and, thus, they are widely used [13,14].

Recently, a new design of a three-component external multi-part strain gauge balance, intended for studying the galloping of solar trackers, has been proposed [15,16]. Due to its relevant characteristics, as different load ranges in different directions and high-frequency response, this balance has been identified as potentially attractive to test airfoils. Furthermore, its reduced size, scalability and ease of manufacturing make it even more interesting for this application.

This work presents a brand-new application of the aforementioned balance, including the testing of its capabilities, and the validation of its use for the evaluation of aerodynamic performance of VAWT airfoils. For that purpose, several prototypes have been tested in a wind tunnel using the balance, including a typical airfoil (DU06-W-200) developed for VAWT applications. Moreover, CFD simulations have been performed with recently developed turbulence models for complementary analysis and comparison.

The paper is structured as follows. Firstly, the experimental set-up used is presented in Section 2, including the description of the wind tunnel, the aerodynamic balance, and measurement procedures. Then, Section 3 describes the main characteristics of the CFD numerical modeling. Afterwards, the validation procedure is presented in Section 4. Two-

and three-dimensional flat plates and the DU06-W-200 airfoil are used for comparison, taking advantage of the available data in the open literature. In Section 5, the results are provided: the validation of the balance against bibliographic results is firstly presented for both the flat plates and the airfoil. In the following section, a deeper analysis is carried out with the help of CFD modelling, including the unsteady phenomena with respect to the pitching angle. Finally, after the presentation of the results, relevant conclusions and future works are provided in Section 6.

2. Experimental Methodology

2.1. Set-Up

This research was conducted in the facilities of the Energy Department of the University of Oviedo (Viesques University Campus at Gijón, Spain). In particular, a subsonic open-loop wind tunnel of 13.75 m in length and powered by a 30 kW axial fan with a diameter of 1.2 m was used for this research. It has a nozzle with a 1:12 area ratio, which provides a squared test section of 0.68×0.68 m^2 and allows wind velocities up to 35.5 m/s. A characteristic turbulence intensity of 0.7% for an averaged integral length scale of 0.1 m was obtained at the nozzle discharge. Although its typical configuration is arranged in an atmospheric, fully opened test section, an additional enlargement of the nozzle sidewalls was made to guarantee planar flow over the tested prototypes (discussed later in detail). A sketch of the wind tunnel is shown in Figure 1a. The test wind velocity is measured from the pressure difference in the nozzle, with a 1 in the H$_2$O $\pm$ 0.25% differential pressure sensor. Note that, given the contraction ratio, velocities in the settling chamber were considered negligible.
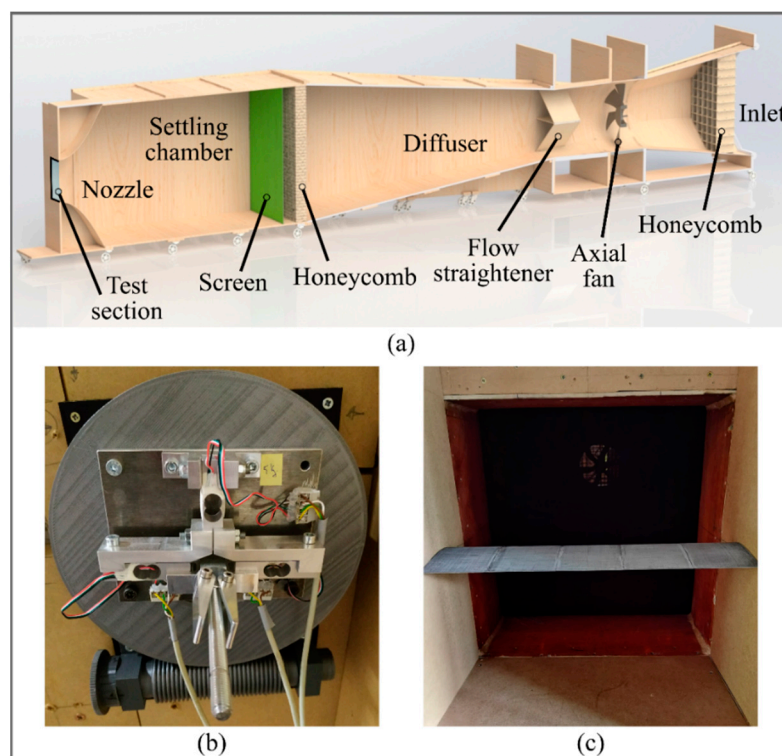

Figure 1. (**a**) Sketch of the wind tunnel (Courtesy of Angie L. Ramírez Celis). (**b**) Aerodynamic balance mounted on the mechanical orientation system. (**c**) DU06-W-200 airfoil prototype in the test section.

The custom-built aerodynamic balance under study is a strain gauge force balance with 3 components, which provides lift and drag forces and pitching moment. This balance was originally conceived to measure unsteady forces and torques on small-scale single-axis solar trackers, and successfully employed for recent aeroelastic investigations in our research

group [15,16]. Precisely, the balance was designed to provide a larger range in one direction with respect to the other, which is also a very useful feature for testing airfoils where lift forces are much greater than drag forces. The balance, which rotates with the prototype to be tested, is composed of a floating axis supported by two symmetrically placed load cells, which are attached to a frame supported by the third load cell. The assembly is designed so that forces and moments outside of the measuring plane are minimized. Two different balances were built for measuring ranges within 0.75 kg and 5 kg, respectively (ranges of the single load cell direction), although the design can be easily scaled to any other quantity. Each load cell has two strain gages that are connected to the same Wheatstone bridge circuit to provide an amplified output. The voltage from the bridges is measured with a data acquisition card, which allows a measuring frequency up to 20 kHz. Note that this is especially relevant when unsteady phenomena are to be studied with this kind of device. The rotation of the balance was performed with a mechanical orientation system which granted the variation in the pitching angle using a worm gear pair (Figure 1b). The system was manufactured by fused deposition modelling (FDM) and allowed a minimum angular step of 0.5°. Finally, measurement data analysis and calculations were performed with custom MATLAB codes in a computer.

Three different prototypes were tested in the aerodynamic balance for this work: two flat plates (of different dimensions) and the DU06-W-200 airfoil (Figure 1c). One of the flat plates was designed to perform as a theoretical 3D plate, featuring an aspect ratio (L/c, where L is the span and c is the chord or width) of 3.2, which was proved to be sufficient for the purpose. On the other hand, the 2D plate had a span as wide as the wind tunnel test section (a clearance of tenths of a millimeter was left so that there is no contact with the walls) and the same width of the 3D flat plate. Note that this allowed testing both at the same wind velocity with an equal Reynolds number. Hence, the 2D flat plate had an aspect ratio of 7.2. The airfoil prototype also had a span as wide as the wind tunnel, but the chord was chosen so that, at the objective Reynolds, the obtained forces were coherent with the range of the aerodynamic balance used. Thus, the resultant aspect ratio was 3.8, which, given the results obtained, proved to be sufficient to obtain 2D airfoil coefficients over this wall-to-wall prototype. The dimensions of the tested prototypes are included in Table 1.

Table 1. Tested prototypes and dimensions.

Prototype	Span [mm]	Chord/Width [mm]	Aspect Ratio [-]
Flat plate 3D	300	95	3.2
Flat plate 2D	680	95	7.2
DU06-W-200	680	180	3.8

The three models were made of PLA and manufactured with FDM, requiring subsequent sanding and polishing to achieve an adequate final roughness. The prototypes have in their core a steel rod to increase their stiffness. This rod has a fixed support connection to the balance and cylindrical joint in the wall of the other end, avoiding movements in the measurement plane and prototype bending. The balance calibration procedure already accounts for the effect of the second support.

2.2. Balance Calibration

In order to provide quality measurements, the aerodynamic balance was calibrated before each experiment. The calibration routine employed for this work assumed a linear response of the load cells, so a direct (exact solution) method was chosen to determine the correlation coefficients. The calibration, which implied a two-stage procedure to determine the calibration matrix, was completed under "no wind" conditions. In the first stage, the prototype was just mounted in the balance and a measurement was performed at free load, defining the zero-loading state. In the second stage, several measurements were performed with the balance loaded with known weights. Specifically, 3 load cases (LC) were carried out:

- Single load, F_{x_1}, in the horizontal direction (LC1).
- Single load, F_{y_2}, in the vertical direction (LC2).
- Combined load, obtained through a vertical load, F_{y_3}, displaced a known distance b from the axis (LC3).

From each load case, three outputs (one for each load cell) were obtained providing a 9 equation and 9 unknowns system to represent the direct correlation between loads and measured components. Matrix algebra can be applied to streamline this process in the following way.

First, a force matrix F_{LC} is defined with the three load cases, with one column for each component and one row for each load case.

$$F_{LC} = \begin{pmatrix} F_{x_1} & 0 & 0 \\ 0 & F_{y_2} & 0 \\ 0 & F_{y_3} & F_{y_3}b \end{pmatrix} \tag{1}$$

where F is the applied load, x and y are the horizontal and vertical directions, respectively, in the balance coordinate system, and b is the horizontal distance to the axis in load case 3.

With the output of the single load cell being associated with the measurements in the horizontal direction in these experiments, referred to as "signal 1" (s_1), and the other two, associated with the measurements in the vertical direction, referred to as "signal 2" (s_2) and "signal 3" (s_3), the output of the balance in the zero-loading state can be posed as a vector S_{LC_0} containing the values recorded in each load cell.

$$S_{LC_0} = \begin{pmatrix} S_{1_0} & S_{2_0} & S_{3_0} \end{pmatrix} \tag{2}$$

Following this, the matrix S_{LC} is defined with the load cells' output for the three load cases, yielding:

$$S_{LC} = \begin{pmatrix} s_{1,1} & s_{1,2} & s_{1,3} \\ s_{2,1} & s_{2,2} & s_{2,3} \\ s_{3,1} & s_{3,2} & s_{3,3} \end{pmatrix} \tag{3}$$

Then, the calibration matrix K with the coefficients that relate the output of the three load cells with the forces and moment is:

$$K = \begin{pmatrix} k_{1,1} & k_{1,2} & k_{1,3} \\ k_{2,1} & k_{2,2} & k_{2,3} \\ k_{3,1} & k_{3,2} & k_{3,3} \end{pmatrix} \tag{4}$$

Finally, applying the linear response assumption, the equation system is thus stated as:

$$F_{LC} = \left[S_{LC} - S_{LC_0} \right] \cdot K \tag{5}$$

where the no-load signals are discounted as the system offset. From this matrix system, matrix K can be directly deduced as $K = [S - S_0]^{-1} \cdot F_{xyz}$, thus obtaining the direct relation between load cell outputs and measured forces.

Once the calibration matrix is determined, it can be employed to obtain the forces acting on the models from the signals measured during the operation of the wind tunnel using a generalization of Equation (5) for a single-point measurement:

$$F_{xyz} = [S - S_0] \cdot K \tag{6}$$

where F_{xyz} and S are now row vectors with three columns.

As the calibration used is a linear, two-point method, the balance was additionally tested before the aerodynamic measurements' campaign to evaluate its accuracy. Figure 2 shows the response of the calibrated balance (y-axis) to 5 different known weights in the

lower part of the balance range (x-axis), where the linearity of these types of sensors is mostly critical.
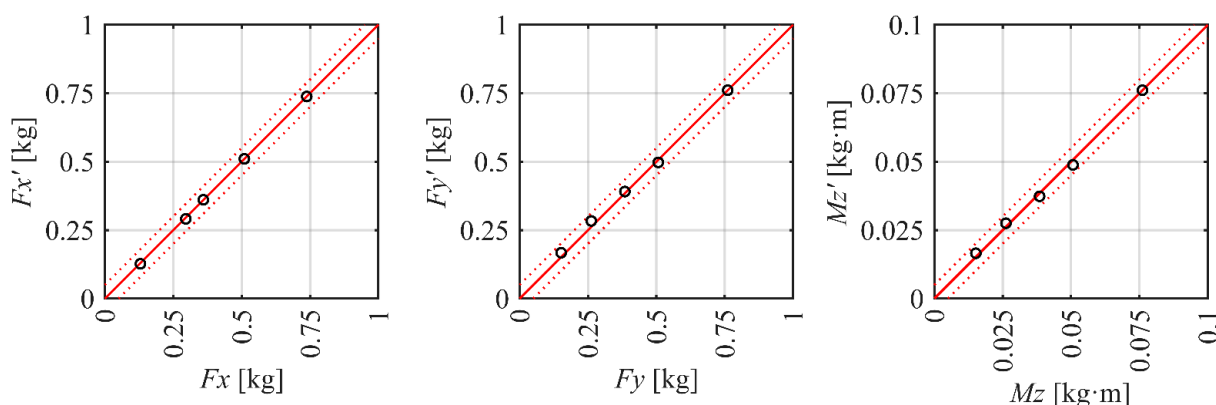

Figure 2. Balance response to a range of known weights using a two-point, linear calibration method.

The figure shows that the calibration method used provides a sufficiently accurate linear response, even for the lower part of the balance range. The response in this range is better in the horizontal direction because its range is half than the others, so it is better prepared to measure small forces. This is especially interesting to the case of airfoil testing, as drag forces are much lower than lift ones.

During the aerodynamic measurements campaign, the balance was calibrated before each experiment and tested after with known weights to validate the balance calibration. This reduces the influence of random errors produced by differences in the testing environment temperature, differences in the set-up assembly, etc. Up to 13 calibrations were performed during the campaign, providing useful statistical data of the balance performance. Table 2 shows the mean, standard deviation, maximum and median value of the relative errors between the known weights and the measured weights those 13 calibrations.

Table 2. Relative error statistics of 13 calibrations performed during the measurements campaign.

Component	Fx	Fy	Mz
$\bar{e}$ [%]	1.31	0.83	1.11
$s(e)$ [%]	1.13	0.86	1.41
e_{max} [%]	3.48	2.74	4.31
$\widetilde{e}$ [%]	0.81	0.40	0.29

The mean relative error obtained was around 1%, slightly higher in the horizontal direction and slightly lower in the vertical direction. However, as the standard deviation reveals, there was some variability in the quality of the calibrations; hence, the mean is not very representative of the real performance of the balance. Note that although all 13 calibrations have been included in this analysis, a quality requirement was established in 1%. Thus, calibrations with errors above this, such as the one that achieved the maximum error shown in Table 2, were discarded and repeated. Nevertheless, as the median indicates, these discarded cases were not common and the typical balance calibration errors were about 0.8% for the horizontal direction, 0.4% for the vertical direction, and 0.3% for the moment. In these calibrations, the loads were adjusted to the expected measured forces; hence, in contrast with the previous figure, the vertical and moment errors are lower. The higher error in the horizontal force is probably due to the higher difficulty to produce a pure horizontal load, as opposed to the simplicity of vertical loading.

2.3. Aerodynamic Measurements

With the balance already calibrated, the procedure for the aerodynamic measurements is as follows. The offset signals S_0 can be equal to S_{LC_0} or not, depending on the chosen

zero-load state of reference. This aspect is especially relevant when a given pitching angle α is fixed for the prototype–balance assembly because S_0 must be measured for every particular pitch. In addition, to obtain the forces F_{DLz} in the wind coordinate system (drag and lift, see Figure 3), a base–change matrix, M_{BC}, must be applied in the following way:

$$M_{BC} = \begin{pmatrix} \cos\alpha & -\sin\alpha & 0 \\ \sin\alpha & \cos\alpha & 0 \\ 0 & 0 & 1 \end{pmatrix} \tag{7}$$

$$F_{DLz} = F_{xyz} \cdot M_{BC} \tag{8}$$
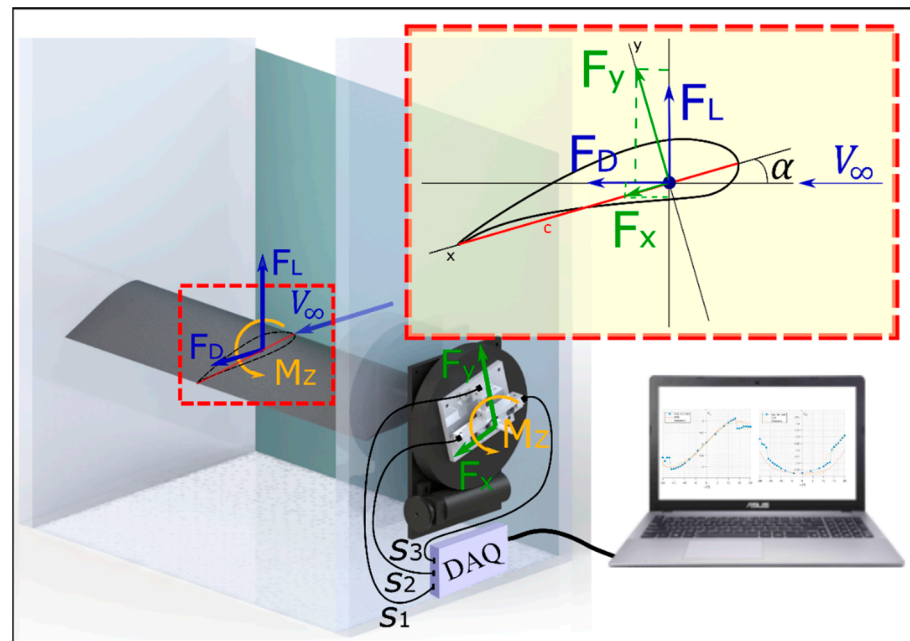
Figure 3. Diagram of the set-up with the variables and the different coordinate systems involved in the measuring procedure.

The aerodynamic coefficients can be finally obtained if the measured forces are made non-dimensional with the upstream dynamic pressure expressed as a force exerted on the prototype:

$$F_\infty = \frac{1}{2}\rho v_\infty^2 c L \tag{9}$$

leading to:

$$C_{DLM} = F_{DL} \cdot \begin{pmatrix} 1/F_\infty & 0 & 0 \\ 0 & 1/F_\infty & 0 \\ 0 & 0 & 1/F_\infty c \end{pmatrix} \tag{10}$$

where ρ is the air density, v_∞ the reference wind velocity, c is the chord/width of the prototype and L its span. The moment component must also be divided by the chord/width again to produce the non-dimensional moment coefficient. Hence, from Equation (10), the drag, lift and moment coefficients are retrieved directly.

The three aforementioned prototypes were tested following this procedure. Particularly, both flat plates were tested at a Reynolds number ($Re_c = v_\infty c/\nu$, where ν is the air kinematic viscosity) of 130,000 from $0°$ to $90°$ of the pitching angle using a constant angular step of $10°$. Complementarily, the airfoil was tested at a Reynolds number of 200,000, going from $-20°$ to $20°$ with a variable angular step, for a better characterization of the aerodynamic forces during the airfoil stall. The three gauge signals were recorded during almost 15 s at a typical acquiring rate of 20 kHz, which assured a sufficient number of points to guarantee correct repeatability and accuracy in the results.

3. Numerical Modelling

A 2D numerical model of the DU-06-W-200 airfoil was implemented in Ansys-FLUENT® v2020 to obtain the aerodynamic coefficients numerically. The Reynolds-averaged Navier–Stokes equations were resolved in an incompressible approach using eddy–viscosity turbulence modelling. Both Spalart–Allmaras (S-A) and new generalized k-ω (GEKO) models were used. The one-equation S-A model [17] is widely used for external aerodynamic applications. Although it is known to provide reasonable solutions for flows with adverse pressure gradients and separation, its accuracy to predict separation is lower than optimal two-equation models such as k-ω omega SST and GEKO. In addition, all k-ω models in Ansys are implemented with a y+-insensitive wall treatment, avoiding the discussion concerning the optimal selection of wall formulations in k-ε models [18].

GEKO is a recent turbulence model framework (based on the ω-equation) which introduces free parameters into the equations. The main advantage is that relevant parameters can be decided and tuned by the user for given operative ranges, and without a negative impact on the basic model calibration. The main tuning parameter for the GEKO model is the coefficient C_{SEP}, which controls the boundary layer separation, predicting a more aggressive detachment if its value is increased. In the case of airfoils, it is highly recommended to use a value between 2.0 and 2.5 [19]. Furthermore, the GEKO model has been executed also with the option for scale-adaptive simulation (SAS) activated, which deploys an improved URANS formulation for the resolution of the turbulent spectrum in unstable flow conditions. The SAS concept is based on the introduction of the von Kármán length scale into the turbulence scale equation, allowing the model to dynamically adjust to resolved structures in a URANS simulation, which results in an LES-like behavior in unsteady regions of the flow field (those with flow separation).

An extended domain, with a distance to the inlet of 12.5c and a distance to the outlet equal to 20c (domain size 32.5$c \times$ 25c), in line with typical values found in the literature, was considered accurate to avoid the effect of the boundaries on the development of the flow inside the domain region (see Figure 4). A C-mesh distribution has been employed around the airfoil, resulting in a [350 $\times$ 75] cell size for both pressure and suction sides of the airfoil. An averaged value of y += 1.7 (at Re_c = 200,000) has been achieved with the first mesh point located at roughly 0.05 mm from the wall. At the wake region, a structured mesh of [300 $\times$ 150] cells was also employed, resulting in 97,500 cells for the complete 2D model. Furthermore, an additional refined mesh with [525 $\times$ 150] nodes on the airfoil walls and 247,500 cells for the whole domain was also employed to check the solution sensitivity to the grid resolution.

The boundary conditions of the simulation domain are given in Figure 4 which includes details of the adopted mesh. A velocity inlet condition of 16.4 m/s was set at the domain inlet to match the Reynolds number (200,000) of the experimental measurements. Furthermore, up to 21 different angles of attack (*AoA*) were simulated to complete a detailed evolution of the aerodynamic coefficients, including negative and positive incidences: $\pm$[0, 2, 4, 6, 8, 10, 12, 14, 16, 18, 20]. According to previous measurements, a turbulence intensity of 0.7% was fixed for a length scale one order of magnitude lower than the characteristic size of the test section in the wind tunnel. Both steady and unsteady simulations have been conducted, the latter necessary at high *AoA* for partially and fully detached flow conditions. A time-step size of 3×10^{-4} s was fixed in order to track the evolution of the vortex shedding with sufficient resolution. A time-averaged value of the airfoil coefficients was finally computed after periodically fluctuating regimes were achieved (typically, 50 times the airfoil chord flow-time).

The flow equations were discretized using the finite volume method with a second-order scheme for momentum and turbulent variables. Second-order accuracy was also selected in the transport equation for the pressure correction. The discretization of the temporal terms (when necessary) corresponds to a bounded second-order implicit formulation. The SIMPLE algorithm was used for the pressure–velocity coupling for all studied cases. Spatial discretization regarding gradient terms was selected to be the least-squares

cell-based discretization. Finally, a convergence criterion of 10^{-6} was fixed for the velocity components of the momentum equation, while a minimum threshold of 10^{-5} was at least required for the rest of the equations. Simulations were performed using a four-node Intel Core i7-52820K at 3.3 GHz and 64 Gb RAM, with characteristic CPU times of 75 min for every execution (1 day of CPU time to complete the whole angular range) in the case of the refined mesh.
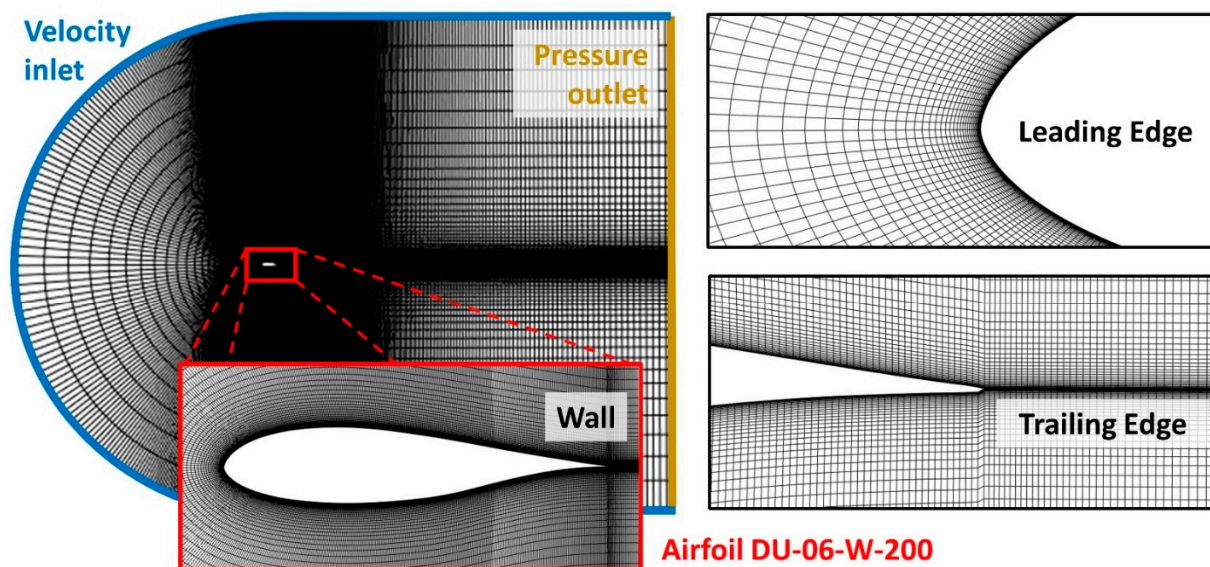

Figure 4. CFD simulation mesh detail views and boundary conditions.

4. Validation Data Sources

4.1. Flat Plate Data

The available data in the bibliography for the lift and drag coefficients in 2D and 3D flat plates have been obtained from [20]. This reference shows how the force on a flat plate can be calculated from the aerodynamic coefficients. The different data are provided for Reynolds numbers greater than 10,000 with an estimated precision of $\pm 5\%$. Specifically, the aerodynamic coefficients on a flat plate of infinite span (2D) were obtained by applying the experimentally modified Kirchhoff and Rayleigh theory of discontinuous motion shown in the works of [21] and [22]. The coefficients for flat plates in three dimensions, presented in the equations shown by Blevins, were originally extracted from the experimental measurements presented by [23].

4.2. DU06-W-200 Airfoil

This airfoil was specifically designed for vertical axis wind turbine applications, with the objective of improving the self-starting abilities of this type of turbine. The available aerodynamic data of the DU06-W-200 airfoil in the literature, used to contrast the obtained results in the present database, are found in [24]. This source provides experimental work performed in the Low Turbulence Tunnel (LTT) at the Technical University of Delft. This wind tunnel has a 1.25×1.8 m test section and can achieve a maximum wind speed of 120 m/s. The tested model was made of solid aluminum with a 1.8 m span (the whole section width) and a chord of 0.25 m, and the aerodynamic coefficients were obtained with a six-component external balance. Two types of results are presented: "clean", corresponding to the bare airfoil in the wind tunnel with around 0.02% turbulence, and "dirty", which is the same testing conditions, but the airfoil features a zig-zag tape at 5% of the chord, simulating a much more turbulent test environment. From the available results, those corresponding to a Reynolds number of 300,000 have been chosen as a reference, as they are the closest to our experimental dataset.

5. Results

In this section, the results of the different tests are presented. Particularly, the results have been divided depending on the type of prototype used in the test: flat plate or DU06-W-200 airfoil.

5.1. Flat Plate

The aerodynamic coefficients (C_D, C_L) obtained with the flat plates are shown in Figure 5, compared with the data from the bibliography. Experimental curves are plotted with red discontinuous lines, using triangles for the 2D flat plate and squares for the 3D flat plate. On the other hand, 2D and 3D flat plate data from the bibliography are plotted with green and blue dotted lines, respectively.
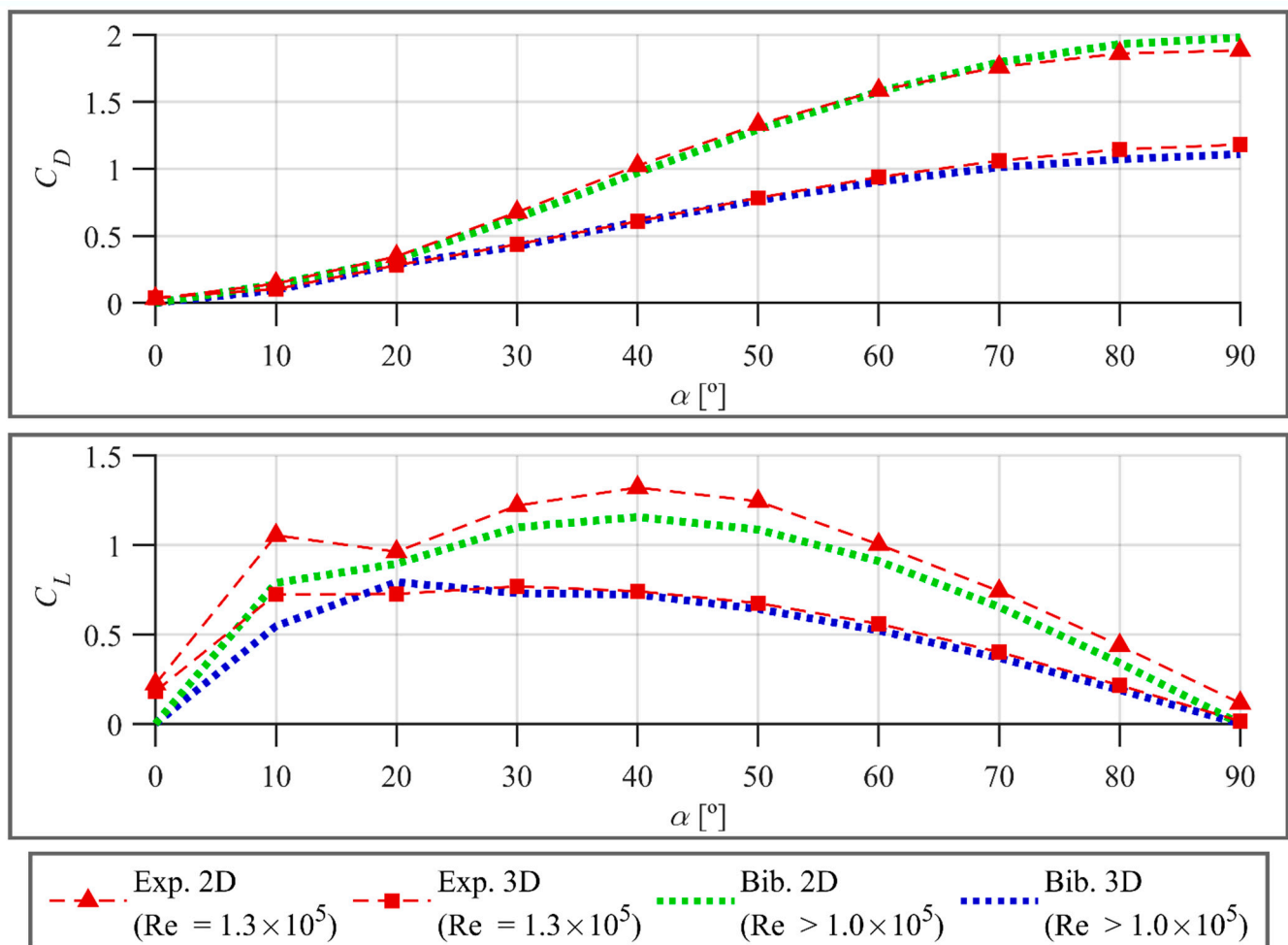
Figure 5. Experimental drag and lift coefficients from 2D and 3D flat plates compared with data from the bibliography.

The drag coefficient (top plot) exhibits a remarkable agreement for both flat plates in the whole angular range, with a very slight drift at high pitching angles. Complementarily, the lift coefficients (bottom plot) also show a good overall agreement, although with some overestimation for angles smaller than 20 degrees. This can be attributed to the lack of a complete symmetry between both pressure and suction sides of the plates. In fact, only the pressure sides are completely flat, because of a slight engrossment of the suction side at the mid-chord to accommodate a sufficiently robust shaft. Thus, at low pitching angles, when the flow is still attached, this geometrical defect raises the pressure difference between both sides leading to an increase in the lift force. However, at higher pitching angles, the flow in the suction side is completely detached and the experimental data matches the reference

data with especially accurate results for the 3D flat plate. Despite the experimental lift coefficients for the 2D flat plate being slightly above the bibliography, the global trend is perfectly reproduced. The overall result suggests an accurate and precise performance of the balance, thus postulating it as a good candidate for airfoil testing.

5.2. DU06-W-200 Airfoil

Figure 6 shows the comparison of the experimental coefficients (C_D, C_L) of the airfoil measured with the aerodynamic balance and the data from the bibliography. Experimental data from this work are plotted with a red discontinuous line and triangle markers. Up to six complete tests were repeated in an effort to properly characterize the hysteresis zone related to the flow separation. Thus, in this figure, the markers and discontinuous line show the averaged coefficients from all the tests, while the light-red area bounds the maximum and minimum dispersion in the results.
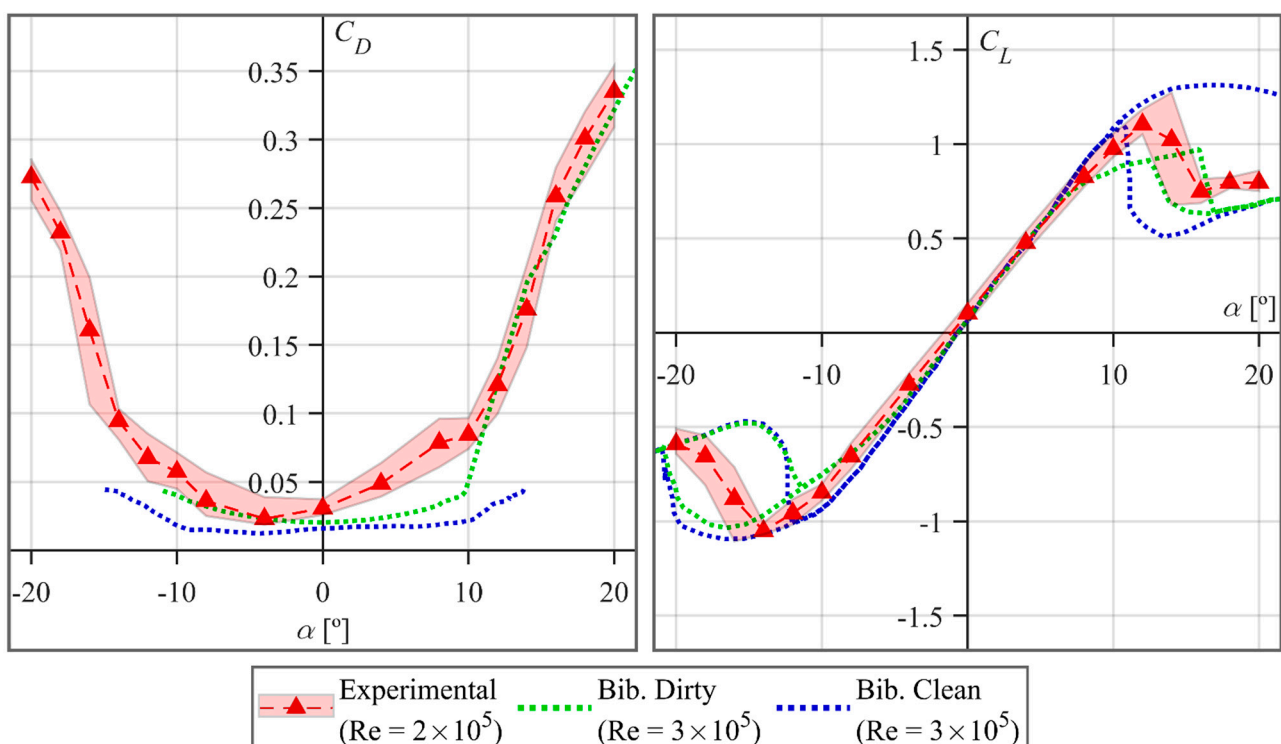
Figure 6. Experimental drag and lift coefficients from airfoil DU06-W-200 compared with data from the bibliography.

Regarding the drag coefficient (left plot), the obtained results are significantly higher than those from the "clean" dataset. This can be easily related to the big difference in the mean turbulence level (about 35 times) between both wind tunnels. Nevertheless, the obtained results match remarkably well for the "dirty" dataset, with the exception of the range of low positive angles, in which the obtained coefficients are higher. The reason of this discrepancy may probably lie in the presence of a light dimple in the airfoil shape, close to the leading edge at the pressure side. This defect is a consequence of the deburring of the seam scar produced in the layer shift as the airfoil is 3D-printed. That irregularity may be triggering turbulence transition on the airfoil (precisely in the stagnation point) and, thus, increasing the drag artificially. Furthermore, additional polishing of the area has also slightly modified the local slope of the airfoil, leading to a mismatch with respect to the original geometry.

Meanwhile, the lift coefficient curves (right plot) overlap perfectly for all the datasets at low pitching angles ($-6°$ to $6°$), where the flow is completely attached, and the incoming flow turbulence is not relevant. However, at higher angles ($-6°$ to $-11°$ and $6°$ to $10°$), the

"clean" dataset bounds the maximum magnitude of the lift, with the obtained experimental results slightly below and the "dirty" dataset starting to decay due to the early flow separation. At negative angles of attack, both "clean" and "dirty" datasets maintain a slow and progressive detachment when the pitching angle is increased, until they finally drop at $-20°$. On the other hand, the experimental data from this work drops earlier at $-16°$, after achieving the maximum magnitude of the negative lift. Although our experiments have in fact not been performed to describe the hysteresis cycles, it is significant that the dispersion of the results resemble that phenomenon to some extent. Hence, the width of the hysteresis loop in the reference data is much higher than in the experiments, which practically crosses through the middle, dividing the others in half. This also occurs with the positive side of the curve. However, here, the difference between the lift drop of the "clean" dataset and the two others is much higher with the first one dropping outside the shown range ($\sim22°$) and the other two around $14°\sim15°$. Furthermore, despite the experimental data achieving almost the same maximum lift coefficient as the "clean" dataset, the drop zone and hysteresis loop width match better the "dirty" dataset. The existence of a boundary layer on the side walls of the tunnel generating 3D effects at the ends of the tested wing may affect the hysteresis of flow separation on the wing. This could be the reason for the observed large differences between the experiment and CFD calculations at large angles of attack.

Considering the overall results, the aerodynamic balance used in this experiment clearly exhibits a notable accuracy, being able to reproduce the reference dataset both in drag and lift coefficients, and clearly characterizing the flow separation.

A further analysis of the experimental data obtained is discussed with the help of the CFD simulations performed. In Figure 7, the experimental coefficients are compared with the results from CFD simulations for different turbulence models and simulating conditions. Specifically, results from the simulation with the Spalart–Allmaras (S-A) model executed in a steady fashion are represented in dark gray, those computed steadily but for a generalized k-ω (GEKO) model are shown in green, whereas the GEKO unsteady simulations are shown in blue, distinguishing between the coarse mesh (light-blue discontinuous line) and the extra refined mesh (dark-blue continuous line).

Despite the simplifications of the S-A steady simulation, it performs remarkably well in reproducing the lift curve, with only a slight underestimation of the maximum. However, it is clearly unable to predict an accurate drag overshoot. On the other hand, the set of GEKO simulations produce subtle different results among them. The GEKO steady simulation significantly improves the results compared with the S-A, accurately characterizing the drag overshoot as well as the lift curve. Nevertheless, it overestimates both drag and lift magnitude at negative wide angles ($-12°$ to $-20°$). The results from the GEKO unsteady simulation and with the coarse mesh are enhanced, but show that the initial mesh is not sufficiently accurate to reproduce the lift curve when flow separation starts to be significant. In fact, it is still poorly predicting important flow features when the airfoil stalls, such as the instabilities of the boundary layers and the shedding of trailing vortexes. This is clearly improved with the extra-refined mesh, which produces the best results, especially for negative angles of attack. Yet, it still fails to predict accurate lift drops in the case of fully detached flow.

Since no data were found in the bibliography for the pitching moment, the experimental results have been directly compared with the GEKO unsteady simulation for the refined mesh in Figure 8. Furthermore, as a preliminary approach to evaluate unsteady capabilities of the aerodynamic balance, the RMS value of the fluctuations in the moment coefficient is also represented (dispersion bars) and compared in the figure. In this case, instead of presenting the averaged statistics of the whole dataset as before, only a single measurement has been used to ensure that these fluctuating results are consistent.
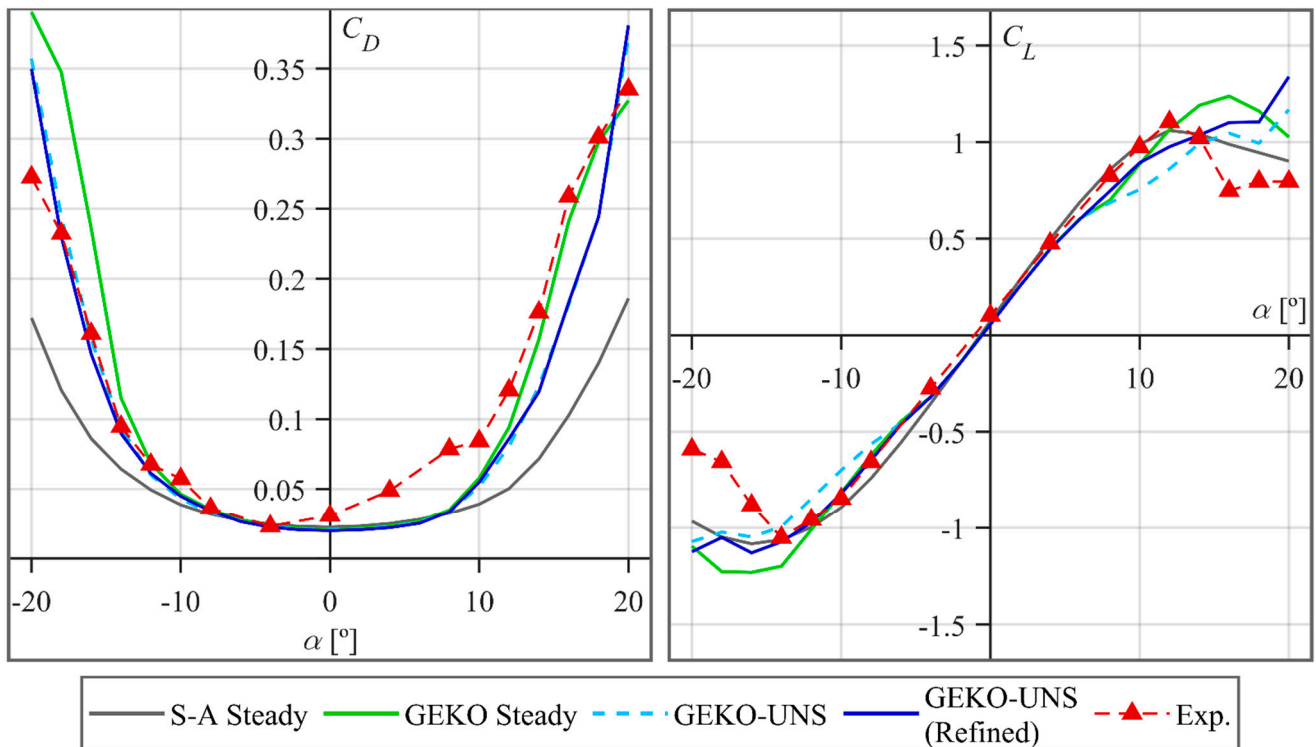
Figure 7. Experimental drag and lift coefficients from airfoil DU06-W-200 compared with results from CFD simulations for different turbulence models.
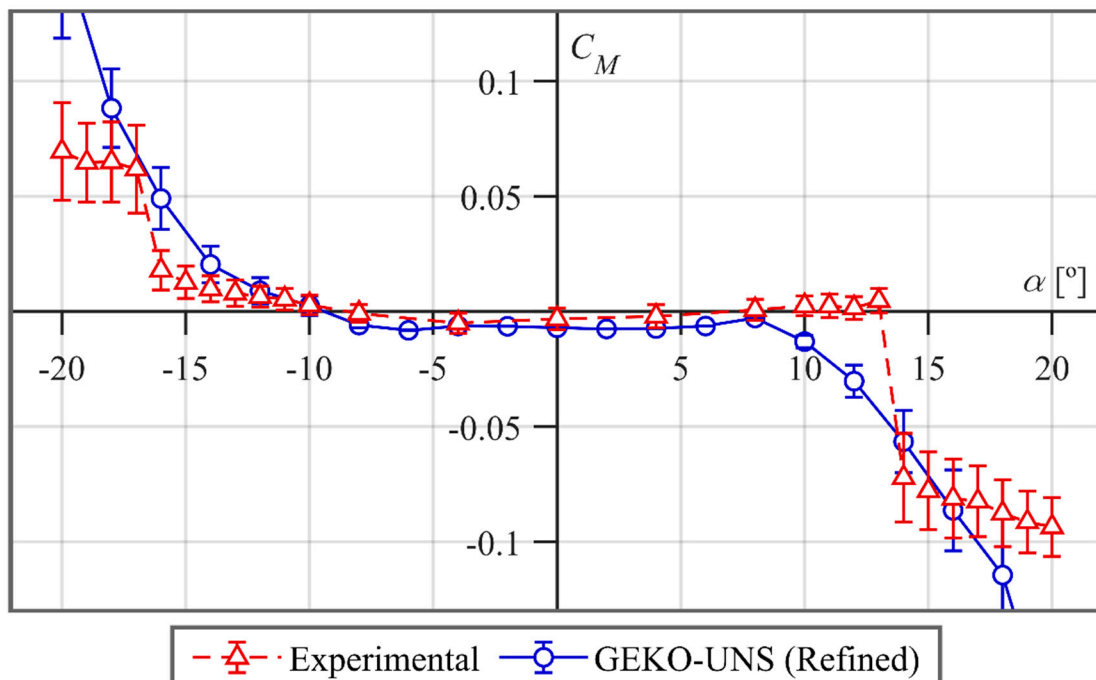

Figure 8. Experimental moment coefficient and fluctuating moment coefficient from airfoil DU06-W-200 compared with results from the best unsteady CFD model.

As expected, the moment coefficient for low pitching angles, which it is practically zero, matches perfectly between experiments and numerical results (solid and dashed lines). This is coherent with the hypothesis of the airfoil having the center of pressure approximately at 25% of the chord (the same location for the origin of coordinates in the

CFD and for the center of the shaft in the experimental prototype). However, as pitching angles increase (both in negative and positive directions), the CFD model predicts a smooth, exponential-like rise in the coefficient magnitude, while the experimental results show a more drastic drop at $-16°$ and $13°$, followed by a moderate, linear-slope increase.

In the case of the RMS values, a very low level can be appreciated in the experimental data at low pitching angles. Likewise, the CFD model converges to a unique solution as there is no unsteadiness in the simulations. The flow separation can be easily identified in the figure by the sudden increase in the fluctuations in the experimental dataset, although in the CFD, there is a more progressive increase. Precisely, it was necessary to activate unsteady computations in the CFD model beyond $±8°$ of AoA to account for the inherent unsteadiness of the detached flow. This comparison also reveals that the dynamic sensitivity of the balance is enough to perceive the amplitude of the fluctuating forces, despite the structural damping of the wing model. Conversely, accurate frequency values are not feasible due to the high stiffness of the set-up, thus avoiding a complete fast response of the measurements.

For a deeper understanding of the unsteady phenomena involved in these fluctuating forces, the velocity field, pressure coefficient (defined as $C_p = 2(p - p_\infty)/\rho v_\infty^2$), and spectra of the fluctuating moment have been analyzed in detail for four positive pitching angles ($8°$, $12°$, $16°$ and $20°$) using the data from the refined GEKO unsteady simulation. The results are shown in Figure 9. The instantaneous velocity field at a particular instant in the simulation is represented on the left part of the figure in non-dimensional terms with respect to the upstream velocity. Meanwhile, on the upper-right plot, the pressure coefficient along the airfoil chord is represented for both suction and pressure sides at that same instant. In addition, shadowed areas have been introduced to illustrate how the coefficient is oscillating during a complete shedding cycle. Finally, on the right lower part, the amplitude and oscillating frequency of the moment coefficient are shown, identifying the peak values.

The maps with the representation of the velocity magnitude allow the identification of the stagnation points in the lower part of the leading edge and show an evident trend towards an early flow separation as the pitching angle is progressively increased, with a remarkable thickening of the boundary layer. A counter-rotating pair of vortices is shed from the airfoil, growing in size as the pitching angle is more pronounced. This vortex shedding is coherent with the frequencies of the fluctuating moment, which show high frequency but low size of the vortex shedding at the lower pitching angles. Conversely, lower frequencies and higher sizes of the vortices are observed at higher angles, once the flow is fully detached. As a consequence, the aerodynamic coefficients are intensively fluctuating with amplitudes up to three times larger than those formed at the separation onset. Regarding the pressure coefficient, there is also a notable increase in the oscillations with the pitching angle, revealed as a progressive build-up of the C_p value in the pressure side, and a shift towards the trailing edge of the airfoil in the suction side. Note that from $12°$ onwards, a wide fluctuation can be observed in the trailing edge due to an oscillatory partial reattachment, which it is also responsible for the periodic variations on both drag and lift coefficients.

Previous assertions are validated by means of the Strouhal number, $St = fL/v_\infty$, which relates the vortex shedding of the large turbulent scales and the frequencies of the fluctuating moment. The frequency values (f) correspond to the first (fundamental) harmonic in the power spectrum of the fluctuations for the torque coefficient (see plot in the bottom right in Figure 9). The characteristic length (L) has been adopted as the maximum value of the integral length scale on the airfoil suction side (see Figure 10 below). The integral scale is estimated from the instantaneous values of the turbulent kinetic energy (k) and the turbulent dissipation rate (ε) according to $L = k^{3/2}/\varepsilon$ [25]. Using the convective inlet velocity (v_∞ = 16.4 m/s), typical values around 0.2 are found (see Table 3) for all the situations considered between 10 deg (partial detachment) and 20 deg (fully detached flow),

which is a characteristic value observed in separation of bluff-bodies at moderate-to-high Reynolds numbers.
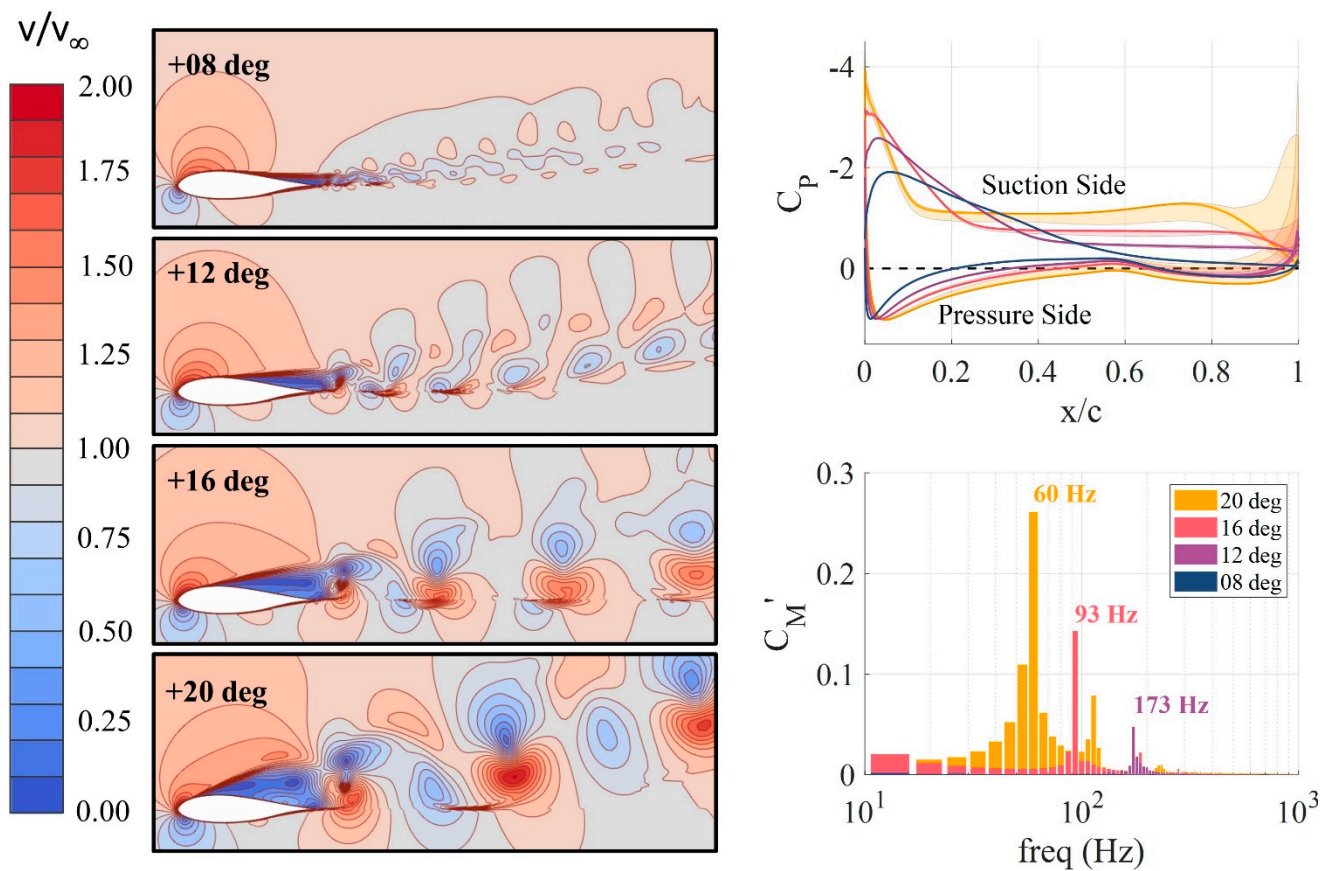

Figure 9. Velocity field, pressure coefficients and spectra of the fluctuating moment at *AoA* = 8°, 12°, 16° and 20°, obtained from the refined GEKO unsteady CFD simulation.

Table 3. Strouhal numbers of the detached flow for different angles of attack.

AoA	f [Hz]	L [m]	St
10 deg	233	0.014	0.197
12 deg	173	0.019	0.199
14 deg	126	0.024	0.185
16 deg	93	0.032	0.180
18 deg	73	0.036	0.160
20 deg	60	0.039	0.143

Figure 10 shows the computed values of integral length scales in the waked regions of the airfoil for different angles of attack. The figure reveals the vortical motion of the largest vortices, identified in a dark-blue color for an instantaneous snapshot, which illustrates the typical turn-out time of the vortices. At a low *AoA*, the size of the vortices is roughly in the order of magnitude of the airfoil thickness, with an intense vortex shedding (high frequency) revealed through the advection transport of the vortices street. For a high *AoA*, the vortices are progressively enlarged, now with a size in the order of magnitude of the airfoil chord, but with a lower shedding frequency (the generation rate of these large flow structures is significantly reduced as shown again in the convective transport along the airfoil wake).
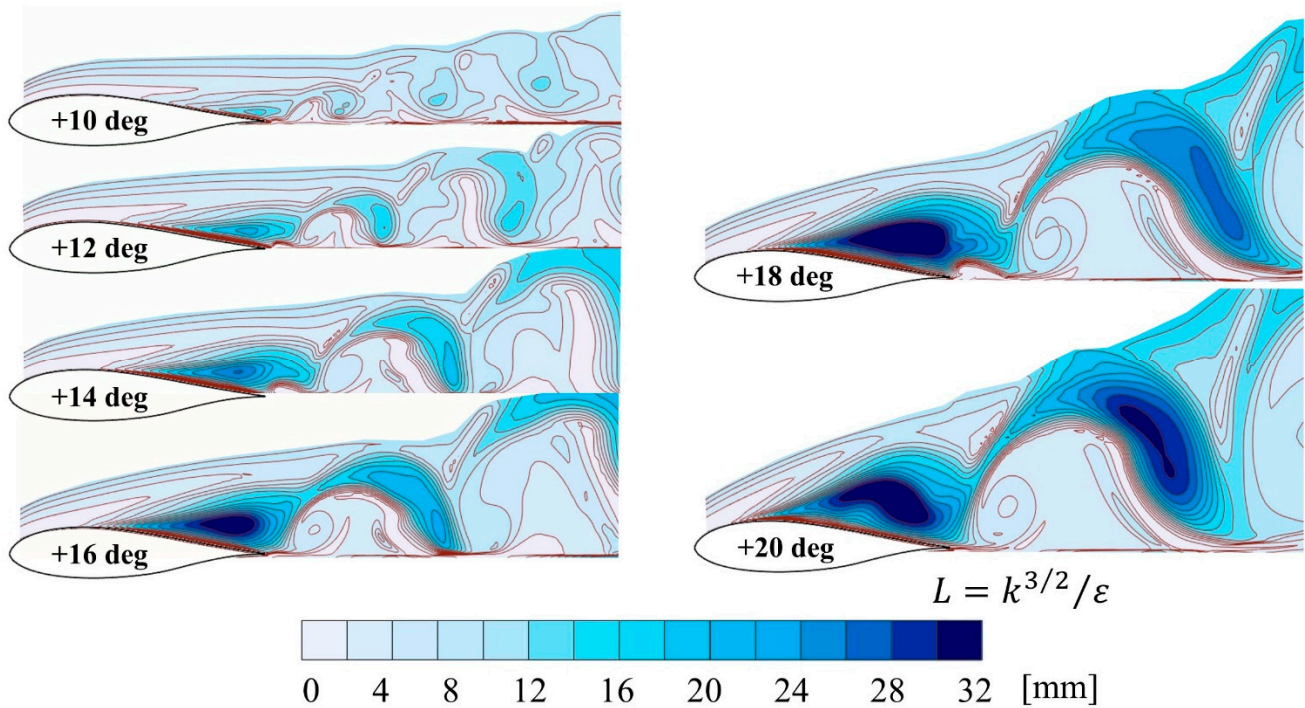
Figure 10. Integral length scales in the airfoil wake for positive *AoA* = 10°, 12°, 14°, 16°, 18° and 20°.

Further insight is now provided with a closer look to the detached regions of the airfoil suction side during a complete oscillation cycle. For that purpose, the longitudinal distribution of the mean pressure coefficients on the suction side of the airfoil is shown in a contour plot in Figure 11, for all the angles-of-attack simulated. A black dashed line identifies the averaged position of the separation point, revealing the severe engrossment of the detached region towards the leading edge for high pitching angles. Moreover, the contour map is complemented by a comprehensive view of the averaged detached regions over the airfoil, for *AoA* going from 6° to 20° (right plot), in order to illustrate the recirculation zones (identified with negative streamwise velocities).
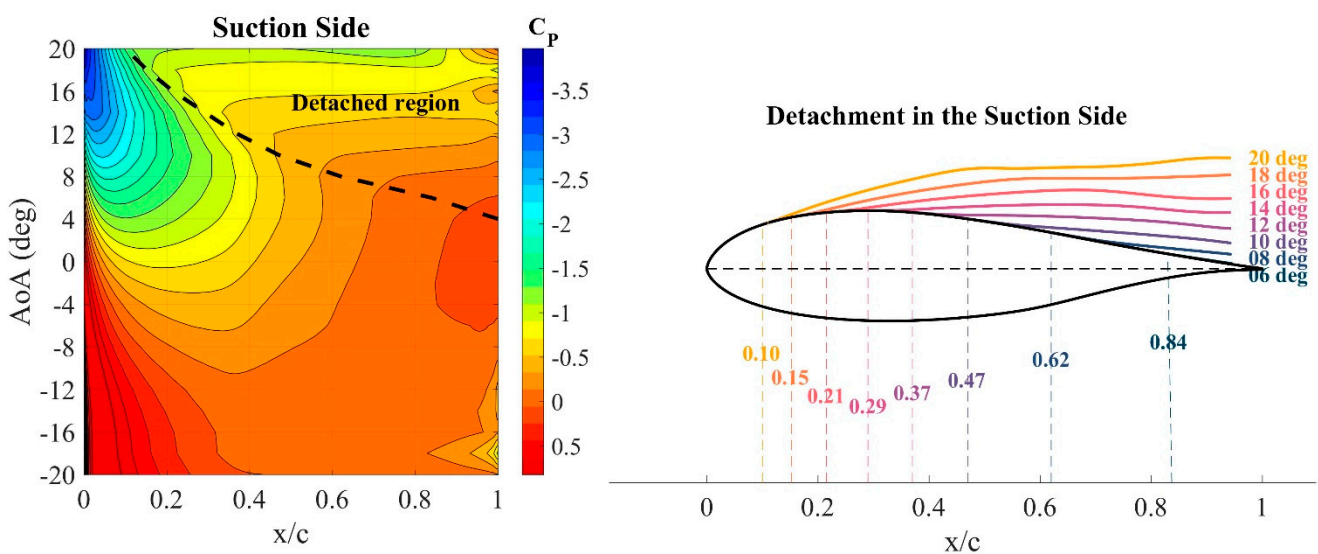
Figure 11. Pressure coefficient in the suction side, boundary layer and flow detachment point, for a wide set of pitching angles simulated with the refined GEKO unsteady model.

As expected, the position of the detachment point (where the wall shear stress equals zero) moves towards the leading edge, leaving a growing detached region. Note that at 20°, more than 80% of the suction face is exposed to fully detached flow. Although not shown here for brevity, a similar contour map is obtained for the pressure side, but symmetrically flipped with respect to the zero *AoA* and with a small shift, as detachment occurs at slightly higher angles for this side.

6. Conclusions

2D and 3D flat plates, in addition to the DU06-W-200 airfoil, have been tested in a wind tunnel equipped with a new external balance, designed for the measurement of aerodynamic forces. The inherent features of the balance make it suitable for an accurate characterization of VAWT airfoils, although specific validation has been required to ensure its performance. Furthermore, CFD simulations of the airfoil have been performed with different turbulence models and flow conditions, complementing the experimental results, and illustrating vividly the unsteady phenomena involved.

The experimental drag and lift coefficients obtained for both the flat plates and DU airfoil match the data available in the literature remarkably well, even at large angles of attack, when unsteady flow is rather relevant. The studied balance has proved its ability to capture fluctuating forces, although noise-filtering procedures must be implemented to obtain more reliable instantaneous data.

The new GEKO turbulence model used for this work offers accurate predictions of forces and moment, providing the best results when running unsteadily in the case of detached conditions, although the mesh requirements are significantly higher with respect to the steady simulations.

Finally, in light of the obtained results, the balance design as well as the CFD models have been successfully validated, and their integrated use has proved to be a highly recommendable and useful approach to test new airfoil geometries or airfoils featuring flow augmentation devices for VAWT applications.

References

1. IEA. *Net Zero by 2050—A Roadmap for the Global Energy Sector*; IEA: Paris, France, 2021.
2. Kumar, R.; Raahemifar, K.; Fung, A.S. A Critical Review of Vertical Axis Wind Turbines for Urban Applications. *Renew. Sustain. Energy Rev.* **2018**, *89*, 281–291. [CrossRef]
3. Hand, B.; Kelly, G.; Cashman, A. Aerodynamic Design and Performance Parameters of a Lift-Type Vertical Axis Wind Turbine: A Comprehensive Review. *Renew. Sustain. Energy Rev.* **2021**, *139*, 110699. [CrossRef]

4. Balduzzi, F.; Bianchini, A.; Carnevale, E.A.; Ferrari, L.; Magnani, S. Feasibility Analysis of a Darrieus Verti-cal-Axis Wind Turbine Installation in the Rooftop of a Building. *Appl. Energy* **2012**, *97*, 921–929. [CrossRef]

5. Du, L.; Ingram, G.; Dominy, R.G. A Review of H-Darrieus Wind Turbine Aerodynamic Research. *Proc. Inst. Mech. Eng. C J. Mech. Eng. Sci.* **2019**, *233*, 7590–7616. [CrossRef]

6. Barnes, A.; Marshall-Cross, D.; Hughes, B.R. Towards a Standard Approach for Future Vertical Axis Wind Tur-bine Aerodynamics Research and Development. *Renew. Sustain. Energy Rev.* **2021**, *148*, 111221. [CrossRef]

7. Micallef, D.; van Bussel, G. A Review of Urban Wind Energy Research: Aerodynamics and Other Challenges. *Energies* **2018**, *11*, 2204. [CrossRef]

8. Zhao, Z.; Wang, D.; Wang, T.; Shen, W.; Liu, H.; Chen, M. A Review: Approaches for Aerodynamic Performance Improvement of Lift-Type Vertical Axis Wind Turbine. *Sustain. Energy Technol. Assess.* **2022**, *49*, 101789. [CrossRef]

9. Howell, R.; Qin, N.; Edwards, J.; Durrani, N. Wind Tunnel and Numerical Study of a Small Vertical Axis Wind Turbine. *Renew Energy* **2010**, *35*, 412–422. [CrossRef]

10. Selig, M.S.; McGranahan, B.D. Wind Tunnel Aerodynamic Tests of Six Airfoils for Use on Small Wind Turbines. *J. Sol. Energy Eng. Trans. ASME* **2004**, *126*, 986–1001. [CrossRef]

11. Wang, Z.; Zhuang, M. Leading-Edge Serrations for Performance Improvement on a Vertical-Axis Wind Turbine at Low Tip-Speed-Ratios. *Appl. Energy* **2017**, *208*, 1184–1197. [CrossRef]

12. Kamliya Jawahar, H.; Alihan Showkat Ali, S.; Azarpeyvand, M.; Ilário da Silva, C.R. Aerodynamic and Aeroa-coustic Performance of High-Lift Airfoil Fitted with Slat Cove Fillers. *J. Sound Vib.* **2020**, *479*, 115347. [CrossRef]

13. Tropea, C.; Yarin, A.L.; Foss, J.F. *Handbook of Experimental Fluid Mechanics*; Springer: Berlin, Germany, 2007.

14. Tavakolpour-Saleh, A.R.; Setoodeh, A.R.; Gholamzadeh, M. A Novel Multi-Component Strain-Gauge External Balance for Wind Tunnel Tests: Simulation and Experiment. *Sens. Actuators A Phys.* **2016**, *247*, 172–186. [CrossRef]

15. Martínez-García, E.; Marigorta, E.B.; Gayo, J.P.; Navarro-Manso, A. Experimental Determination of the Resistance of a Single-Axis Solar Tracker to Torsional Galloping. *Struct. Eng. Mech.* **2021**, *78*, 519–528. [CrossRef]

16. Martínez-García, E.; Blanco-Marigorta, E.; Parrondo Gayo, J.; Navarro-Manso, A. Influence of Inertia and Aspect Ratio on the Torsional Galloping of Single-Axis Solar Trackers. *Eng. Struct.* **2021**, *243*, 112682. [CrossRef]

17. Spalart, P.R.; Allmaras, S.R. One-Equation Turbulence Model for Aerodynamic Flows. *Rech. Aerosp.* **1994**, 5–21. [CrossRef]

18. Menter, F.; Sechner, R.; Germany GmbH Matyushenko, A.A.; Petersburg, S. Best Practice: RANS Turbulence Modeling in Ansys CFD. 2019. Available online: https://fluidcodes.ir/rans-turbulence-modeling/ (accessed on 27 July 2022).

19. Menter, F.R.; Matyushenko, A.; Lechner, R. Development of a Generalized K-ω Two-Equation Turbulence Model. *Notes Numer. Fluid Mech. Multidiscip. Des.* **2020**, *142*, 101–109. [CrossRef]

20. Blevins, R.D. *Applied Fluid Dynamics Handbook*; Van Nostrand Reinhold Co.: New York, NY, USA, 1984.

21. Bradford Wick, B.H.; June, W. *Study of the Subsonic Forces and Moments on an Inclined Plate of Infinite Span*; UNT Libraries Government Documents Department: Denton, TX, USA, 1954.

22. Fage, A.; Johansen, F.C. On the Flow of Air behind an Inclined Flat Plate of Infinite Span. *Proc. R. Soc. Lond. Ser. A Contain. Pap. A Math. Phys. Character* **1927**, *116*, 170–197. [CrossRef]

23. Goldstein, S. (Ed.) *Modern Developments in Fluid Mechanics*; Oxford University Press: London, UK, 1938.

24. Claessens, M.C. The Design and Testing of Airfoils for Application in Small Vertical Axis Wind Turbines. Master's Thesis, Delft University, Delft, The Netherlands, 2006.

25. Pope, S.B. *Turbulent Flows*; Cambridge University Press: Cambridge, UK, 2000.